Discrete Simulation of Gas-Liquid Bubble Columns and Gas-Liquid-Solid Fluidized Beds

Caixia Chen and Liang-Shih Fan
Dept. of Chemical Engineering, The Ohio State University, Columbus, OH 43210

A computational scheme for three-dimensional (3-D), discrete simulation of bubble dynamics in gas-liquid bubble columns and gas-liquid-solid fluidized beds is presented. This scheme describes the motion of the gas, liquid, and solid phases, respectively, based on the level-set interface tracking method, the locally averaged time-dependent Navier-Stokes equations coupled with the Smagorinsky Sub-Grid Scale stress model, and the Lagrangian particle motion equations. Various gas, liquid, and solid interactive forces are considered, which include those due to drag, added mass, interfacial tension, bubble-particle collision and particle-particle collision. The accuracy and validity of the simulation based on this scheme is examined through computational experiments on some well-known bubbling phenomena including the rise behavior of a single gas bubble in liquids and the bubble formation process from an orifice embedded in liquids. The computed bubble rise velocity, bubble shapes and their fluctuations, and bubble formation behavior in liquids show a good agreement with existing theories and experimental findings. The simulation is extended to investigate the effects of solids concentration on bubble formation and rise behavior. It is found that the bubbles are less coalesced in a fluidized bed with a higher solids concentration. A circulatory motion of particles with an upward flow in the center region and a downward flow near the wall, and a lateral solids concentration distribution in a gas-liquid-solid fluidized bed can also be predicted. The bubble formation and rise behavior in a multi-nozzle bubble column are simulated, and the limitation of the Smagorinsky Sub-Grid Scale stress model is discussed. © 2004 American Institute of Chemical Engineers *AIChE J,* 50: 288–301, 2004
Keywords: computational fluid dynamics, discrete simulation, gas-liquid-solid fluidization, bubbling phenomena, level-set method

Introduction

Gas-liquid bubble columns and gas-liquid-solid fluidized beds are widely used in the chemical and petrochemical industries. Both flow systems are characterized by the presence of gas bubbles, which induce appreciable liquid mixing and mass transfer. The flows in these systems are represented by two regimes, the homogeneous and the heterogeneous. In the homogeneous regime, the coalescence of bubbles does not occur and there is little variation of bubble sizes. However, this is not the case in the heterogeneous regime. The flow structure in the heterogeneous regime is complex due to substantial coalescence and breakup of bubbles. To qualify and quantify the heat and mass transfer behavior and reactor applications accurately, it is necessary to understand thoroughly the flow structure of these flow systems.

The numerical simulation provides a useful means in the description of the hydrodynamics of the bubbling flows (for example, Grevskott et al., 1996; Lapin and Lübbert, 1994; Sokolichin and Eigenberger, 1994, 1999; Delnoij et al., 1997; Mudde and Simonin, 1999). The numerical modeling of the hydrodynamics of gas-liquid flows generally employs two

Correspondence concerning this article should be addressed to L.-S. Fan at Fan.1@osu.edu.

methods: the Eulerian-Eulerian (E-E) and the Eulerian-Lagrangian (E-L) methods. In the E-E method (for example, Sokolichin and Eigenberger, 1994, 1999; Mudde and Simonin, 1999), both the continuous liquid phase and the dispersed bubble phase are treated as interpenetrating continua, occupying the same space based on the concept of volume averaging, with different velocities and volume fractions for each phase. In this method, the closure relationships for interactive forces between the bubble phase and the liquid phase, and between bubbles within the bubble phase, and effective viscosities for both the liquid and the bubble phases are required to be formulated. In the E-L method (for example, Lapin and Lübbert, 1994; Delnoij et al., 1997), on the other hand, liquid is treated as a continuous phase that is described in the Eulerian mode, and bubbles are treated as a dispersed phase that is tracked in the Lagrangian mode. Typically, the grid size used in the liquid flow computation is much larger than the dispersed bubble size, and the dispersed phase can be treated as point sources in the computational cell. Through this method, the coupling of the continuous phase and the dispersion phase can be formulated using the Particle-Source-In-Cell method (Crowe et al., 1977).

In principle, convergent numerical solutions based on the E-E and the E-L methods are equivalent, although the E-L method is usually more computationally intensive than the E-E method due to the requirement of tracking the motion of a large number of dispersed bubbles for a convergent profile of bubble volume fraction. However, recent research indicates that numerical diffusion caused by coarse grid sizes and large integration time steps used in the E-E method can corrupt the numerical simulation results (Sokolichin et al., 1997). Thus, the E-L method is considered to be more effective in simulating the gas-liquid bubbling flows in this regard.

Both the E-E and the E-L methods have proven to be more effective in modeling the homogeneous regime than the heterogeneous regime of gas-liquid flow. In the simulation of the heterogeneous regime of gas-liquid flows using either the E-E or the E-L method, the challenge lies in the establishment of an accurate closure relationship on the interphase momentum exchange. The interphase momentum exchange is induced through the drag force that liquid exerts on the bubble surface, the virtual mass force due to the bubble and liquid inertial motion, and the lift force caused by the shear flows around the bubbles. In gas-liquid bubble columns and gas-liquid-solid fluidized systems, the interfacial forces under the bubble coalescence and breakup conditions are not well established. A computational model based on the interface tracking methods given below provides some information on the much needed closure relationship of the interphase momentum exchange noted above.

Interface Tracking Methods

There are various methods of interface tracking reported in the literature, including the fixed grid, the moving grid, or the grid-free methods (Scardovelli and Zaleski, 1999). The fixed-grid method, which is known as the continuous-interface method, employs structured or unstructured grids with the interface cutting across the fixed grids. It treats the system as one single flow with density and viscosity varied smoothly across a finite-thickness of the interface. In the moving-grid method, which is known as the discontinuous-interface method, the interface is a boundary between two sub-domains of the grid (Dandy and Leal, 1989). The grid may be structured or unstructured and even near-orthogonal, moving with the interface (Hirt et al., 1974). It treats the system as two distinct flows separated by a surface. When the interface undergoes large deformation, the grid will need to be re-meshed (McHyman, 1984). The remeshing can be a very complicated process, especially when it involves a significant topology change. For methods in which grids are not needed, representatives are the marker particle method (Harlow and Welch, 1965) and the smoothed particle hydrodynamics method (Monaghan, 1994).

Among the three interface tracking methods, the fixed-grid method is the most frequently used due to its relative ease in programming. The fixed-grid method includes the front tracking method (Unverdi and Tryggvason, 1992a,b) and the volume-tracking method (Kothe and Rider, 1995). The front tracking method uses surface-marker particles to track the location of the interface. High-order interpolation polynomials are employed to ensure a high degree of accuracy of the representation of the interface. A surface grid is introduced within a volumetric grid to track the bubble front within the computational domain. Thus, discretization of the field equations is carried out on two sets of embedded meshes: (a) the Eulerian fluid grid, which is 3-D, cubical, staged structured, and nonadaptive; and (b) the Lagrangian front grid, which is 2-D, triangular, unstructured, and adaptive (Unverdi and Tryggvason, 1992a,b). The infinitely thin boundary can be approximated by a smooth distribution function of a finite thickness of about three to four grid spacing. The variable density Navier-Stokes equations can then be solved by conventional Eulerian techniques (Unverdi and Tryggvason, 1992a,b). However, the method can be numerically stiff as the density ratio of the gas to liquid increases. Further, this method may pose difficulties when the appearance, the connection, the detachment, and the disappearance of the gas-liquid interface are encountered. Such interface behavior occurs in the coalescence, breakup, or formation of bubbles in an unsteady flow. The front-tracking method is, therefore, computationally intensive. The volume-tracking method, on the other hand, is the Eulerian treatment of the interface, including the volume of fluid (VOF) method (Kothe and Rider, 1995) and the level-set method (Sussman et al., 1994). In the VOF method, an indicator function is defined as: 0 for a cell with pure gas, 1 for a cell with pure liquid, and 0 to 1 for a cell with a mixture of gas and liquid. An interface exists in those cells that give a VOF value of neither 0 nor 1. Since the indicator function is not explicitly associated with a particular front grid, an algorithm is needed to reconstruct the interface. This is not an easy task especially for a complex dynamic interface requiring 3-D calculation. The level-set method is more amenable to this task, particularly in locating the gas-liquid boundary in 3-D space. In this study, the level-set technique (Sussman et al., 1994) is employed to describe the motion of 3-D gas-liquid interfaces. In what follows, a brief description of this technique is given.

Level-Set Method for Interface Tracking

While similar to the VOF method, the level-set method also uses an indicator function to track the gas-liquid interface on the Eulerian grid. Instead of using the marker particles or

points to describe the interface, a smooth level-set function is defined in the flow field (Sussman et al., 1994). The value of the level-set function is negative in the gas region and positive in the liquid region, while the interface Γ is simply described as the zero level set of the level-set function ϕ, that is

$$\Gamma = \{\mathbf{x} | \phi(\mathbf{x}, t) = 0\} \tag{1}$$

where $\boldsymbol{x}$ represents position vector and t the time. Taking $\phi < 0$ as being inside the bubble (in the gas phase) and $\phi > 0$ as being outside the bubble (in the liquid phase), the level-set function has the form

$$\phi(\boldsymbol{x}, \boldsymbol{t}) \begin{cases} <0, & \boldsymbol{x} \in \text{gas bubble} \\ =0, & \boldsymbol{x} \in \Gamma \\ >0, & \boldsymbol{x} \in \text{liquid} \end{cases} \tag{2}$$

The evolution of ϕ in a flow field is given by

$$\frac{\partial \phi}{\partial t} + V \cdot \nabla \phi = 0 \tag{3}$$

where $\boldsymbol{V}$ is the velocity of fluid, and is given by

$$\boldsymbol{V} = \begin{cases} \boldsymbol{V}_g, & x \in \text{gas} \\ \boldsymbol{V}_g = \boldsymbol{V}_l, & x \in \Gamma \\ \boldsymbol{V}_l, & x \in \text{liquid} \end{cases} \tag{4}$$

V_g and V_l are the gas and liquid velocities, respectively. The zero level set of ϕ from Eq. 3 marks the bubble interface which moves with time.

For the simulation of a gas-liquid bubble column, the liquid velocity distribution outside the bubble and the gas velocity distribution inside the bubble can be obtained by solving the Navier-Stokes equations for the single phase as given by

$$\frac{\partial \rho}{\partial t} + \nabla \cdot (\rho \boldsymbol{V}) = 0 \tag{5}$$

$$\frac{\partial \rho \boldsymbol{V}}{\partial t} + \nabla \cdot (\rho \boldsymbol{V}\boldsymbol{V}) = -\nabla p + \nabla \cdot \boldsymbol{\tau} + \rho \boldsymbol{g} + \boldsymbol{F}_\sigma \tag{6}$$

where F_σ is the surface tension force which is calculated by (Brackbill et al., 1992)

$$\boldsymbol{F}_\sigma = \sigma \boldsymbol{K}(\phi) \delta(\phi) \nabla \phi \tag{7}$$

$\boldsymbol{K}(\phi)$ is the curvature which can be estimated as $\nabla \cdot (\nabla \phi / |\nabla \phi|)$. A smooth δ function is defined as (Sussman et al., 1998; Sussman and Fatemi, 1999)

$$\delta_\beta(\phi) \equiv \frac{dH_\beta(\phi)}{d\phi} = \begin{cases} \frac{1}{2}(1 + \cos(\pi\phi/\beta))/\beta, & |\phi| < \beta \\ 0, & \text{otherwise} \end{cases} \tag{8}$$

where $H_\beta(\phi)$ follows the Heaviside formulation (Sussman et al., 1998; Sussman and Fatemi, 1999) given by

$$H_\beta(\phi) = \begin{cases} 1 & \phi > \beta \\ 0 & \phi < -\beta \\ \frac{1}{2}\left(1 + \frac{\phi}{\beta} + \frac{1}{\pi}\sin(\pi\phi/\beta)\right) & \text{otherwise} \end{cases} \tag{9}$$

The surface tension force F_σ in Eq. 7 is smoothed and distributed into the thickness of the interface. In order to circumvent the numerical instability, the fluid properties such as density and viscosity in the interface are determined with a continuous transition

$$\rho(\phi) = \rho_g + (\rho_l - \rho_g) H_\beta(\phi) \tag{10}$$

$$\mu(\phi) = \mu_g + (\mu_l - \mu_g) H_\beta(\phi) \tag{11}$$

Since the values for $\rho(\phi)$, $\mu(\phi)$ and the surface tension force could be distorted if the variation of $\nabla\phi$ along the interface is very large, the thickness of the interface needs to be maintained uniform, that is, $|\nabla\phi| = 1$ (Sussman et al., 1998). In the algorithm developed, the general level set function $\phi(\mathbf{x}, t)$ is replaced by a distance function $d(\mathbf{x}, t)$, whose value represents the signed normal distance from x to the interface. $d(\mathbf{x}, t)$ would satisfy $|\nabla d| = 1$ and $d = 0$ for $x \in \Gamma$ (Sussman et al., 1998).

Even if the initial value of the level-set function $\phi(\mathbf{x}, 0)$ is set to be the distance function, the level set function ϕ may not remain as a distance function at $t > 0$ when the advection equation Eq. 3, is solved for ϕ. Thus, a re-distance scheme is needed to enforce the condition of $|\nabla\phi| = 1$. An iterative procedure was designed (Sussman et al., 1998) to reinitialize the level set function at each time step so that the level set function remains as a distance function while maintaining the zero level set of the level set function. This is achieved by solving for the steady-state solution of the equation (Sussman et al., 1994, 1998; Sussman and Fatemi, 1999)

$$\frac{\partial d}{\partial \tau} = \text{sign}(\phi)(1 - |\nabla d|) \tag{12}$$

$$d(\mathbf{x}, 0) = \phi(\mathbf{x}) \tag{13}$$

until

$$|\nabla d| = 1 + O(\Delta^2) \tag{14}$$

where the sign function is defined as

$$\text{sign}(\phi) = \begin{cases} -1, & \phi < 0 \\ 0, & \phi = 0 \\ 1, & \phi > 0 \end{cases} \tag{15}$$

In Eq. 12, τ is an artificial time that has the unit of distance. The solutions for Eq. 12 are signed distances and only those within a thickness of 3—5 grid sizes from the interface are of interest (Sussman et al., 1994, 1998; Sussman and Fatemi, 1999). Equation 12 needs to be integrated for 3—5 time steps using a time step $\Delta\tau = 0.5\Delta$.

Numerical Procedure for Solving the Gas-Liquid Interface

The numerical procedures for solving the gas-liquid interface include the solution of the time-dependent Eqs. 3—6. Given ϕ_n and V_n defined at cell centers at one time instant t_n, ϕ_{n+1} and V_{n+1} can be solved over a time increment at a new time instant $t_{n+1} = t_n + \Delta t$ following the procedure given below:

(1) Solve Eqs. 5 and 6 to obtain the velocity distribution in the flow field V_{n+1} using the Arbitrary-Lagrangian-Eulerian (ALE) scheme (Kashiwa et al., 1994).

(2) Solve Eq. 3 to obtain ϕ_{n+1} using the second-order TVD-Runge-Kutta method presented as follows

$$\bar{\phi}_{n+1} = \phi_n + \Delta t \phi_{tn} \tag{16}$$

$$\phi_{n+1} = \phi_n + \frac{\Delta t}{2}(\bar{\phi}_{tn+1} + \phi_{tn}) \tag{17}$$

where $\phi_{tn} = -V_n \nabla \phi_n$ and the time steps are the same as that used in calculating V_{n+1}, which is determined by restrictions due to the Courant-Friedrichs-Levy (CFL) condition, gravity, viscosity and surface tension.

(3) Solve Eq. 12 to perform the re-distance.

Although, in principle, Eq. 12 does not yield a variation on the position of the zero level set of ϕ, in practice, for numerical computation, this may not be true. A re-distance operation is needed to maintain the volume conserved. Therefore, Eq. 12 is modified as (Sussman et al., 1998)

$$\frac{\partial d}{\partial \tau} = \text{sign}(\phi)(1 - |\nabla d|) + \lambda_{ij} f(\phi) \equiv L(\phi, d) + \lambda_{ij} f(\phi) \tag{18}$$

where

$$\lambda_{ij} = \frac{-\int_{\Omega_{ij}} H'(\phi) L(\phi, d)}{\int_{\Omega_{ij}} H'(\phi) f(\phi)} \tag{19}$$

and

$$f(\phi) \equiv H'(\phi)|\nabla \phi| \tag{20}$$

Governing Equations for the Gas-Liquid-Solid Flow

The gas-liquid-solid flow is characterized by a wide range of physical length scales, including small to large eddies in the bubble wake, and size in mm for solid particles and in mm $\sim$ cm for gas bubbles. The accurate description of the gas bubble surface and bubbling flow requires the use of fine grids, while the tracking of the motion of solid particles needs the grid size to be much larger than the particle sizes.

For the simulation of a gas-liquid-solid fluidized bed, the locally averaged Navier-Stokes equations (Anderson and Jackson, 1967) are used to describe the liquid phase flow outside the gas bubble, and the gas-phase flow inside the gas bubble. Due to the large grid size used, the liquid-phase turbulence needs to be considered. In this study, a modified coefficient that illustrates the effect of the bubble-induced turbulence for a Sub-Grid Scale (SGS) stress model is employed. The level-set method and the numerical procedures described earlier are used to simulate the motion and the topological variation of the gas bubble. The locally averaged governing equations of Eqs. 5 and 6 for liquid flow outside the bubble and gas flow inside the bubble are given as

$$\frac{\partial \varepsilon \rho}{\partial t} + \nabla \cdot (\varepsilon \rho \boldsymbol{V}) = 0 \tag{21}$$

$$\frac{\partial \varepsilon \rho \boldsymbol{V}}{\partial t} + \nabla \cdot (\varepsilon \rho \boldsymbol{V}\boldsymbol{V}) = -\varepsilon \nabla p + \varepsilon \nabla \cdot \boldsymbol{\tau} - \varepsilon \nabla \cdot \boldsymbol{\tau}^{sg} + \varepsilon \rho \boldsymbol{g} + \boldsymbol{F}_D + \varepsilon \boldsymbol{F}_\sigma \tag{22}$$

ε represents the void fraction of liquid or gas and satisfies

$$\varepsilon + \varepsilon_p = 1 \tag{23}$$

where ε_p is the void fraction of solid particles. τ^{sg} is the SGS stress term. It is modeled by the Smagorinsky (1963) model written as

$$\boldsymbol{\tau}_{ij}^{sg} = -\nu_T \left(\frac{\partial \boldsymbol{V}_i}{\partial x_j} + \frac{\partial \boldsymbol{V}_j}{\partial x_i} \right) \tag{24}$$

where ν_T is defined as

$$\nu_T = (C_s l)^2 |S| \tag{25}$$

for bulk flow, and

$$\nu_T = C_s f(y) l^2 |S| \tag{26}$$

for walls with a wall function $f(y)$. C_s is the Smagorinsky coefficient, $l = \Delta$ and

$$|S| \equiv \sqrt{2 S_{ij} S_{ij}} \tag{27}$$

The volumetric fluid-particle interaction force F_D in Eq. 22 is calculated from the forces acting on the individual particles in a cell

$$\boldsymbol{F}_D = -\frac{\sum f_d^k}{\Delta \Omega_{ij}}, \tag{28}$$

where f_d is the fluid-particle interaction force for a single particle and $\Delta\Omega$ is the cell volume.

Modeling the Motion and Collision Dynamics of Solid Particles in Gas-Liquid-Solid Fluidization

The motion of a particle in the flow field can be described in the Lagrangian coordinate with the origin placed at the center of the moving particle. There are two modes of the particle motion, translation and rotation. Interparticle collisions result in both the translational and the rotational movement, while the fluid hydrodynamic forces cause particle translation. Assuming that the force acting on a particle can be determined exclusively from its interaction with the surrounding liquid and gas, the motion of a single particle without collision with other particle can be described by Newton's second law as

$$\frac{d\boldsymbol{x}_p}{dt} = \boldsymbol{V}_p \tag{29}$$

$$m_p \frac{d\boldsymbol{V}_p}{dt} = m_p \boldsymbol{g} + \frac{\pi}{6} d_p^3(-\nabla p + \nabla \cdot \boldsymbol{\tau} - \nabla \cdot \boldsymbol{\tau}^{sg}) + \boldsymbol{f}_{dr} + \boldsymbol{f}_{am} + \boldsymbol{f}_{\sigma} \tag{30}$$

where x_p and V_p are the particle position and particle velocity, respectively, and d_p is the diameter of the particle. The five terms on the righthand side of Eq. 30 represent, respectively, the gravity force, the fluid stress gradient force, the total drag force, the added mass force, and the bubble surface tension induced force. The Saffman, the Magnus, and the Basset forces are ignored.

Note that the lubrication effect due to particle collisions in liquid is significant. The liquid layer dynamics pertaining to the lubrication effect was examined by Zenit and Hunt (1999). Zhang et al. (1999) used the Lattice-Boltzmann (LB) simulation to account for a close-range particle collision effect and developed a correction factor for the drag force for close-range collisions, or the lubrication effect. Such a term has been incorporated in a 2-D simulation based on the VOF method (Li et al., 1999). Equation 30 does not consider the lubrication effect. Clearly, this is a crude assumption. However, in the three-phase flow simulation, this study is intended to simulate only the dilute solids suspension condition (ε_p = 0.42%—3.4%, as will be seen in Figures 12 and 13) with the bubble flow time of less than 1 s starting when bubbles are introduced to the solids suspension at a prescribed ε_p. The particle collision effect under this simulation condition, therefore, would be small.

Note that depends on the manner in which the drag force and buoyancy force are accounted for in the decomposition process for the total fluid-particle interaction force; different forms of the particle motion equation may be involved (Jackson, 2000). In Eq. 30, the total fluid-particle interaction force is considered to be decomposed into two parts: a drag force (f_{dr}) and a fluid stress gradient force (see Eq. 2.29 in Jackson (2000)). The drag force can be related to that expresses by the Wen-Yu equation, $f_{Wen\text{-}Yu}$ by

$$\boldsymbol{f}_{dr} = \boldsymbol{f}_{Wen\text{-}Yu} \tag{31}$$

The Wen and Yu (1966) equation is given by

$$\boldsymbol{f}_{Wen\text{-}Yu} = \frac{1}{8} \pi d_p^2 C_D \varepsilon^2 \rho |\boldsymbol{V} - \boldsymbol{V}_p|(\boldsymbol{V} - \boldsymbol{V}_p) \tag{32}$$

where the effective drag coefficient C_D is calculated by

$$C_D = C_{D0} \varepsilon^{-4.7} \tag{33}$$

In Eq. 33, C_{D0} is a function of the particle Reynolds number, $Re_p = \rho \varepsilon d_p |\boldsymbol{V} - \boldsymbol{V}_p|/\mu$. For rigid spherical particles, the drag coefficient C_{D0} can be estimated by the following equations (Rowe and Henwood, 1961)

$$C_{D0} = \begin{cases} \dfrac{24}{\mathrm{Re}_p}(1 + 0.15(\mathrm{Re}_p)^{0.687}), & \mathrm{Re}_p < 1{,}000 \\ 0.44, & \mathrm{Re}_p \geq 1{,}000 \end{cases} \tag{34}$$

The added mass force accounts for the resistance of the fluid mass that is moving at the same acceleration as the particle. Neglecting the effect of the particle concentration on the virtual mass coefficient, for a spherical particle, the volume of the added mass is equal to one-half of the particle volume, so that

$$\boldsymbol{f}_{am} = \frac{1}{12} \pi d_p^3 \rho \left(\frac{D\boldsymbol{V}}{Dt} - \frac{D\boldsymbol{V}_p}{Dt} \right). \tag{35}$$

When particles approach the gas-liquid interface, the surface tension force acts on the particles through the liquid film. The bubble surface tension induced force can be described by

$$f_{\sigma} = \frac{\pi}{6} d_p^3 \sigma K(\phi) \delta(\phi) \nabla \phi \tag{36}$$

When the particle inertial overcomes the surface tension-induced force, the particle will penetrate the bubbles. Recognizing that particle penetration may not lead to bubble breakage, details of bubble instability due to particle collision are given in Chen and Fan (1989a,b).

To simulate the particle-particle collision, the hard-sphere model, which is based on the conservation law for linear momentum and angular momentum, is used. Two empirical parameters, a restitution coefficient of 0.9 and a friction coefficient of 0.3, are utilized in the simulation. In this study, collisions between spherical particles are assumed to be binary and quasi-instantaneous. The equations, which follow those of molecular dynamic simulation, are used to locate the minimum flight time of particles before any collision. Compared to the soft-sphere particle-particle collision model, the hard-sphere model accounts for the rotational particle motion in the collision dynamics calculation; thus, only the translational motion equation is required to describe the fluid induced particle motion. In addition, the hard-sphere model also permits larger time steps in the calculation; therefore, the simulation of a sequence of collisions can be more computationally effective. The details of this approach can be found in the literature (Hoomans et al., 1996; Crowe et al., 1998).

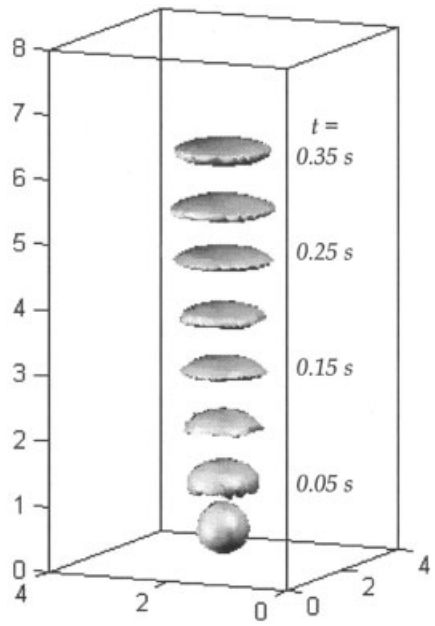

Figure 1. Simulated positions and shape variations of a rising bubble in a water column.

Initial bubble diameter 0.8 cm and time increment 0.05 s.

Results and Discussions

The computation performed in this study is based on the model equations presented earlier. These equations are incorporated into a 3-D hydrodynamic solver CFDLIB, developed by the Los Alamos National Laboratory (Kashiwa et al., 1994). In what follows, simple cases including a single air bubble rising in water and bubble formation from a single nozzle in bubble columns are first simulated. To verify the accuracy of the model, experiments are also conducted for these cases and the experiment results are qualitatively or quantitatively compared with the simulation results. Simulations are performed to account for the bubble rise phenomena in liquid-solid suspensions with single nozzles. Finally, the interactive behavior between bubbles and solid particles is examined. The bubble formation and rising from multiple nozzles are simulated, and the limitation of the applicability of the models is discussed.

Single air bubble rising in water

The simulation for a single air bubble rising in water (density: 0.998 g/cm^3; viscosity: 0.001 Pa · s; surface tension: 0.0728 N/m) is performed in a $4 \times 4 \times 8$ cm^3 3-D column. A uniform grid size of 0.05 cm is used for three dimensions which generates $80 \times 80 \times 160$ ($=1.024 \times 10^6$) grid points in the computational domain. Initially, a spherical air bubble is positioned at rest in this domain with its center located 0.5 cm above the bottom and the liquid is quiescent. The free slip boundary conditions are imposed on all six walls. Note that the dimension of the computational domain is selected based on numerical experiments. It is found that, under both free-slip and no-slip wall boundary conditions, when the distance of the bubble interface to the wall is more than twice as large as the bubble diameter, there is practically of little effect of the wall boundary conditions on the simulation results. Thus, with an exception of the cases involving several bubbles which migrate to the near-wall region through the zigzag motion, as will be discussed in the later section, the simulation results obtained in this study are not affected by these wall boundary conditions. The time for an air bubble of 0.8 cm in diameter rising from the initial position to the outlet of the column is about 0.4 s, which corresponds to a bubble rise velocity of 18.75 cm/s. The simulation is conducted in a Cray SV1 supercomputer at Ohio Supercomputer Center. The CPU time to compute the entire process of bubble rising is 4 h.

The simulation results for the positions and the shape changes of the 0.8 cm air bubble rising in water are shown in Figure 1. The value for the Eötvös number ($Eo = g\Delta\rho d_e^2/\sigma$) and the Morton number ($M = g\mu^4\Delta\rho/\rho^2\sigma^3$) are 8.5 and 2.5×10^{-7}, respectively. The time increment between two bubbles in Figure 1 is 0.05 s. As seen in the figure, the bubble shape undergoes continuous changes from a sphere initially to an oblate ellipsoidal cap, and fluctuates between an oblate ellipsoidal cap and a spherical cap. The rectilinear motion of bubble in water exhibited in the figure occurs for the first several fractions of a second of a single bubble rising (with symmetric wakes) in a quiescent liquid even though the bubble Reynolds number (Re_b) is at the wake shedding regime ($Re_b > 400$). The computed results obtained in this study capture such phenomena well. The liquid field disturbance would eventually induce asymmetric wake yielding wake shedding phenomena of the rising bubble. The behavior of the shape deformation and the flow field around the bubble, and the cross sectional velocity distributions inside and outside the bubble, are shown in Figure 2. In the figure, the velocities of the flow field are obtained by subtracting the rise velocity of the bubble (18.75 cm/s) from the absolute velocity. In this simulation, the initial liquid velocity is set as zero. As the gas bubble rises, a downward flow of the surrounding liquid velocity is observed. Since the velocity fields for both the gas liquid phase are solved simultaneously, the velocity distributions inside and outside the bubble are obtained concurrently. As noted earlier, a finite thickness for the gas-liquid interface and a smooth transition for the physical properties are considered. A no-slip condition is imposed at the bubble surface to obtain a continuous variation of the fluid velocity. The presence of a closed wake and a pair of intense vortex flows behind the bubble is clearly seen

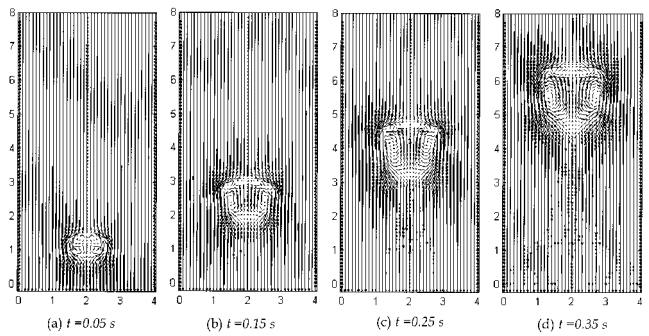

Figure 2. Cross-sectional velocity distribution inside and outside the rising bubbles for four time instants shown in Figure 1 (obtained by subtracting 18.75 cm/s from the simulated velocity).

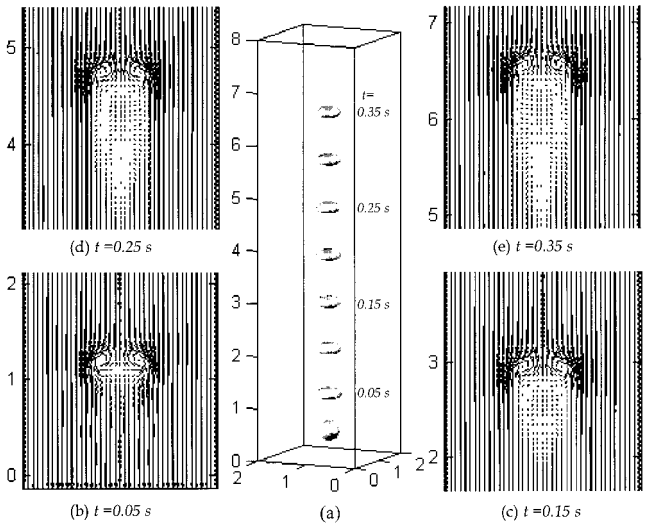

Figure 3. (a) Simulated positions and shape variations of a rising bubble in a water column: initial bubble diameter 0.4 cm and time increment 0.05 s; (b)—(e) cross sectional velocity distribution inside and outside the rising bubble for four time instants shown in (a) (obtained by subtracting 15 cm/s from the simulated velocity).

from the figure. When Figure 1 is compared with Figure 2, it is found that the bubble deforms severely with the increase in the wake size. Also, the wake is highly unsteady, featuring continuous variation in the size and the intensity of the vortex flow, which accompanies the continuous fluctuation of bubble shapes.

The simulation is repeated for a 0.4 cm dia. air bubble in a $2 \times 2 \times 8$ cm^3 3-D column with $Eo = 2.1$ and $M = 2.5 \times 10^{-7}$. The results are shown in Figure 3, where the time increment between two bubbles is the same as in Figure 1. Also shown in this figure are velocity distributions inside and outside the bubble at four time instants (that is, 0.05, 0.15, 0.25, and 0.35 s, respectively). The rise velocity for this case is slightly higher than that for the 0.8 cm bubble, while the bubble shapes are very different. Compared to the 0.8 cm bubble, the wake size for 0.4 cm bubble is much smaller, the wake vortex flow is relatively weak, and the bubble deformation is less significant. The velocity distributions are obtained here by subtracting a lower rising velocity (15 cm/s) from the absolute velocity, which then reveals a pair of vortex flows inside the bubble.

The mesh refinement studies are conducted to examine the mesh effect on the computation results. Simulations of a 0.8 cm air bubble rising in a $4 \times 4 \times 8$ cm^3 water column (as shown in Figures 1 and 2) are repeated at three different mesh resolutions: from a lower resolution of $40 \times 40 \times 80$ grid points with a grid size of 0.1 cm to a higher resolution of $100 \times 100 \times 200$ grid points with a grid size of 0.04 cm. The simulated variations of bubble rise velocity and bubble aspect ratio (height/width) with time are shown in Figures 4a and 4b, respectively.

Figure 4a indicates that the bubble rise velocity measured based on the displacement of the top surface of the bubble (U_{bt}) quickly increases and approaches the terminal bubble rise velocity in 0.02 s. The small fluctuation of U_{bt} is caused by the numerical instability. The bubble rise velocity measured based on the displacement of the bottom surface of the bubble (U_{bb}) fluctuates significantly with time initially and converges to U_{bt} after 0.25 s. The overshooting of U_{bb} can reach 45—50 cm/s in Figure 4a. The fluctuation of U_{bb} reflects the unsteady oscillation of the bubble due to the wake flow and shedding at the base of the bubble. Although the relative deviation between the simulation results of the $40 \times 40 \times 80$ mesh and $100 \times 100 \times 200$ mesh is notable, it is insignificant between the results of the $80 \times 80 \times 160$ mesh and those of the $100 \times 100 \times 200$ mesh. The agreement with experiments at all resolutions is generally reasonable, although the simulated terminal bubble rise velocities (~20 cm/s) are slightly lower than the experimental results (21 ~ 25 cm/s). A lower bubble rise velocity obtained from the simulation is expected due to the no-slip condition imposed at the gas-liquid interface, and

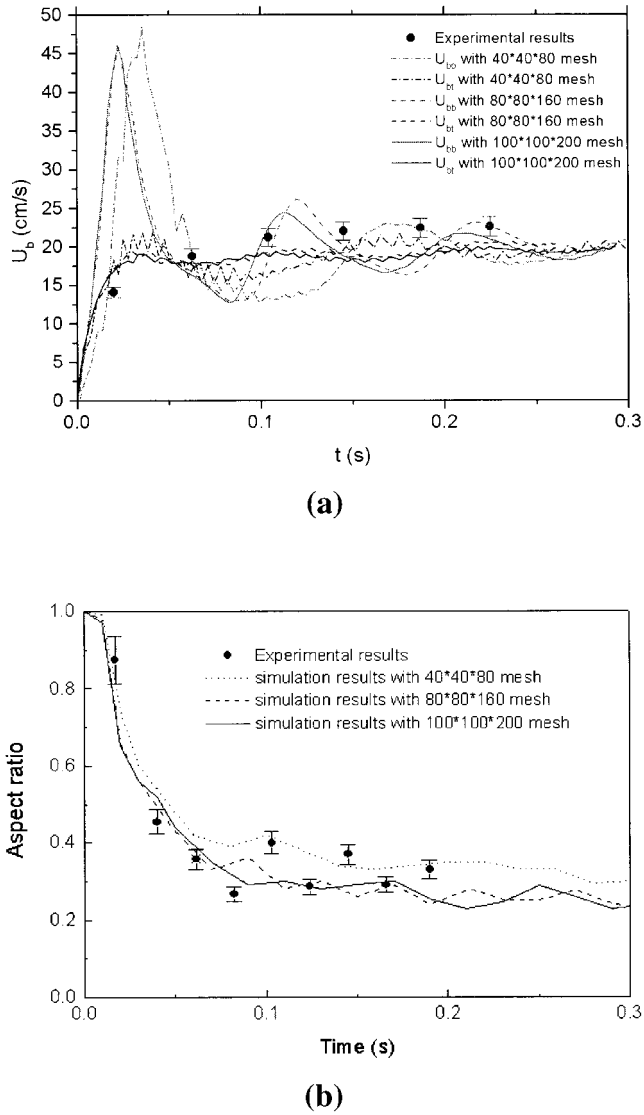

Figure 4. (a) Comparison of the simulation results and experimental results of the bubble rise velocity; (b) comparison of the simulation and experimental results of the bubble aspect ratio.

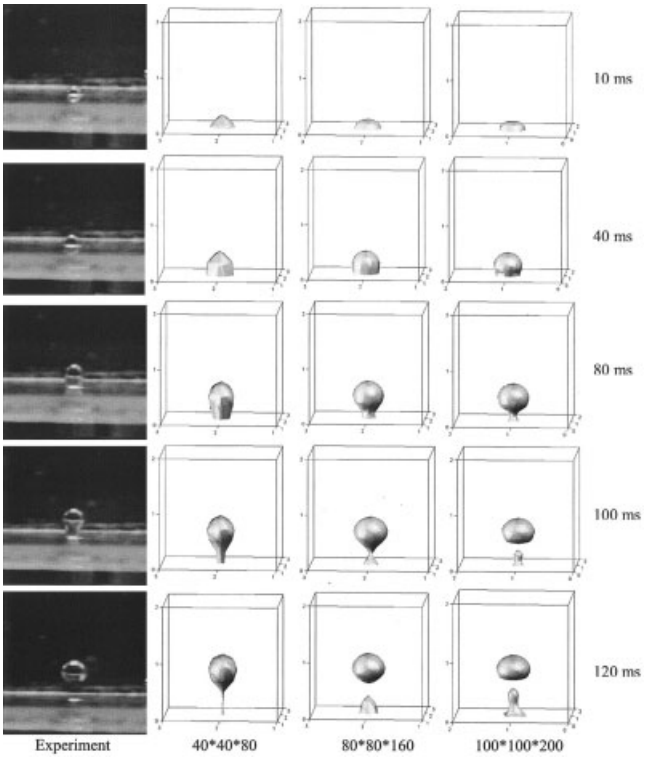

Figure 5. Comparison of the experimental measurement and the simulation results with different resolutions of air bubble formation in water.

the finite thickness for the gas-liquid interface employed in the computational scheme.

The aspect ratio shown in Figure 4b describes the change of the bubble shape with time during the bubble rising. The simulation and the experimental results generally agree well as shown in the figure. It can also be seen that the simulation results are only sensitive to the mesh size of $40 \times 40 \times 80$ mesh and the deviation between the results of $80 \times 80 \times 160$ mesh and $100 \times 100 \times 200$ mesh is small. Thus, Figures 4a and 4b indicate that a reasonable accuracy can be reached in this bubble rise simulation with $80 \times 80 \times 160$ mesh (grid size of 0.05 cm).

The simulation results on bubble velocities, bubble shapes, and their fluctuation shown in Figure 4 are consistent with the existing correlations (Fan and Tsuchiya, 1990) and experimental results obtained in this study. Bubble rising experiments are conducted in a 4 cm $\times$ 4 cm Plexiglas bubble column under the same operating conditions as those of simulations. Air and tap water are used as the gas and liquid phases, respectively. Gas is introduced through a 6 mm nozzle. Note that water contamination would alter the bubble rise properties in the surface tension dominated regime. In ambient conditions, this regime covers the equivalent bubble diameters from 0.8 mm to 4 mm. (Fan and Tsuchiya, 1990). All the air-water experiments and simulations of this study are carried out under the condition where most equivalent bubble diameters exceed 4 mm. These flow conditions correspond to the bubble inertial regime, and, thus, the extent of water contamination plays little role in the determination of the bubble rise properties.

The thickness of the gas-liquid interface is set as 3Δ based on the parameters used in the case of Sussman et al. (1998), with the same density-ratio on the interface and a similar Reynolds number. An interface thickness of 5Δ is also examined in the simulation and no significant improvement is observed. The accurate prediction of the bubble shape (shown in Figures 4 and 5) can be attributed, in part, to the manner in which the surface tension force is treated as a body force in the computation scheme. Specifically, since the surface tension force acting on a particle is considered only when a particle crosses the gas-liquid interface and the particle is considered as a point, the accuracy of the calculation of this force can be expected if the surface tension is interpreted as a body force exerting on each of the grid knots near the interface.

Bubble formation from an orifice

The air bubble formation from a single orifice in two different liquids: water and Paratherm NF heat-transfer fluid (density: 0.868 g/cm^3; viscosity: 0.02673 Pa · s; surface tension: 0.0292 N/m) is simulated. Note that the value of the surface tension used in the simulation for the Paratherm NF heat-transfer fluid is obtained from the direct measurements using the technique reported earlier by Li et al. (1999). The computational domain is $2 \times 2 \times 4$ cm^3. For the air-Paratherm system, a uniform grid size of 0.05 cm and $40 \times 40 \times 80$ grid points are used. For the air-water system, however, the resolution are doubled, that is, 0.025 cm grid size and $80 \times 80 \times 160$ grid points, to obtain convergent solutions for the bubble formation process. This mesh size effect is examined by comparing the simulation results on bubble formation processes with experimental measurements. As shown in Figure 5, decreasing the mesh size or increasing the mesh resolution from $40 \times 40 \times 80$ to $80 \times 80 \times 160$ improves the accuracy of the prediction results on the bubble shape. Further increase in mesh resolution does not practically change the simulation results.

Simulations are then performed for gas bubbles emerging from a single nozzle with 0.4 cm I.D. at an average nozzle velocity of 10 cm/s. The experimental measurements of inlet gas injection velocity in the nozzle using a FMA3306 gas flow meter reveal an inlet velocity fluctuation at 3% to 15% of the mean inlet velocity. A fluctuation of 10% is imposed on the gas velocity for the nozzle to represent the fluctuating nature of the inlet gas velocities. The initial velocity of the liquid is set as zero. An inflow condition and an outflow condition are assumed for the bottom wall and the top walls, respectively, with the free-slip boundary condition for the side walls.

Figure 6 shows the simulated formation and rise behavior of air bubbles in Paratherm NF heat-transfer fluid. The bubble

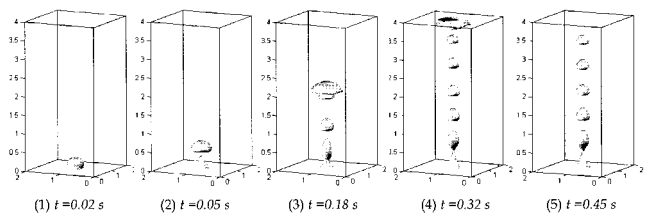

Figure 6. Simulation results of air bubble formation from a single nozzle in Paratherm NF heat-transfer fluid.

Nozzle size 0.4 cm I.D. and nozzle gas velocity 10 cm/s.

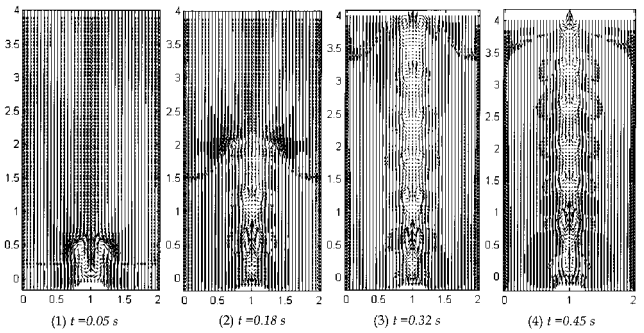

Figure 7. Cross-sectional velocity distributions inside and outside the rising bubbles including those in the bubble formation process shown in Figure 6 (obtained by subtracting 25 cm/s from the simulated velocity).

formation is clearly divided into three stages: expansion, detachment, and deformation. It is noted that the first bubble is much larger than the succeeding bubbles. A strong wake flow formed behind the first bubble and, thus, the first bubble induces local pressure difference, which attracts the trailing bubble to coalescence. Coalescence does not occur for other bubbles formed under the conditions used in this calculation.

The velocity distributions corresponding to Figure 6 are illustrated in Figure 7. This figure is obtained by subtracting a rise velocity of 25 cm/s from the absolute velocity. Except for the first two bubbles, a pair of vortex flows is clearly seen inside the bubble, and each bubble is separated from the wake of the preceding bubble. The figure also shows that a quasi-steady state of bubble formation is achieved after the first bubble bursts out of the computational domain.

Figure 8 shows the simulated air bubble formation and rising behavior in water. The boundary and initial conditions used in this simulation are the same as those in Figures 6 and 7. For the first three bubbles, the formation process is very similar to that in the air-Paratherm system, characterized by three distinct stages of expansion, detachment, and deformation. However, the coalescence of the first two bubbles in the air-water system occurs much later than that in the air-Paratherm system. This is

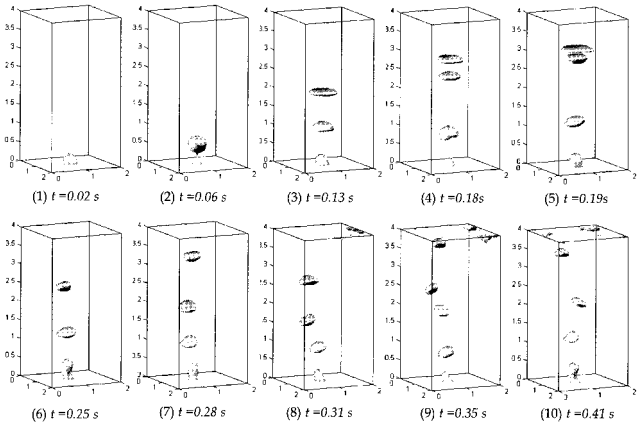

Figure 8. Simulation results of air bubble formation from a single nozzle in water.

Nozzle sizes 0.4 cm I.D. and nozzle gas velocity 10 cm/s.

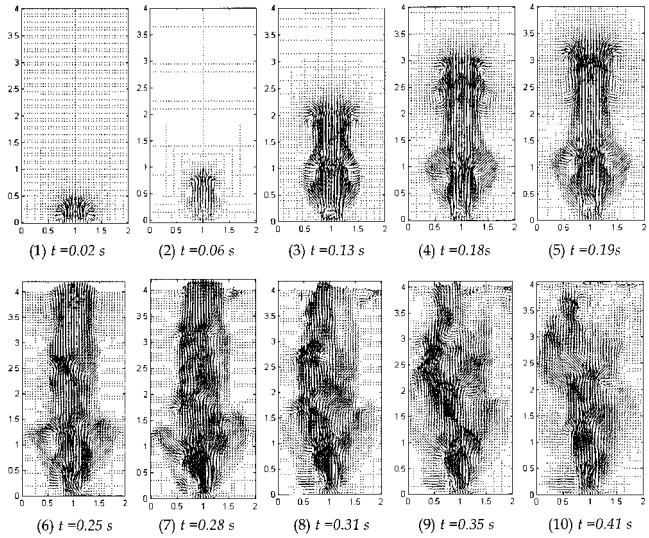

Figure 9. Cross sectional velocity distributions inside and outside the rising bubbles including those in the bubble formation process shown in Figure 8.

due to the fact that, compared to that in the air-Paratherm system, the first bubble in the air-water system is much larger in size and, hence, higher in rise velocity leading to a longer time for its coalescence with the second bubble. Beginning with the third bubble, the formation and rising behavior of the air bubble in water shows strongly asymmetric behavior. As is evident from Figure 8, the bubble rises in a spiral path or a zigzag path. This asymmetric behavior can be clearly observed in the velocity (absolute) distributions illustrated in Figure 9. The figure shows a highly disturbed, unsteady velocity distribution.

In order to verify the simulation results, experiments on bubble behavior in bubble columns are carried out under similar conditions to the simulations. A 3-D rectangular bubble column with the dimension of $8 \times 8 \times 20$ cm^3 is used for the experiments. Four nozzles with 0.4 cm I.D. and a displacement of 2.4 cm are designed and two fluids (water and Paratherm NF heat-transfer fluid) are used in the experiments. For single nozzle experiments, air is injected into the liquid bed through one of the orifices, while the others are shut off. The outlet air velocity from the nozzle is approximated using the measured bubbling frequency and the initial bubble size. A high-speed video camera (240 frames/s) is used to obtain the images of bubbles emerging from the orifice in the liquid.

A common dimensionless number used to characterize the bubble formation from orifices through a gas chamber is the capacitance number defined as: $N_c = 4V_c g\rho_1/\pi D_0^2 P_s$. For the bubble formation system with inlet gas provided by nozzle tubes connected to an air compressor, the volume of the gas chamber is negligible, and, thus, the dimensionless capacitance number is close to zero. The gas-flow rate through the nozzle would be near constant. For bubble formation under the constant flow rate condition, an increasing flow rate significantly increases the frequency of bubble formation. The initial bubble size also increases with an increase in the flow rate. Experimental results are shown in Figures 10 and 11. In Figure 10,

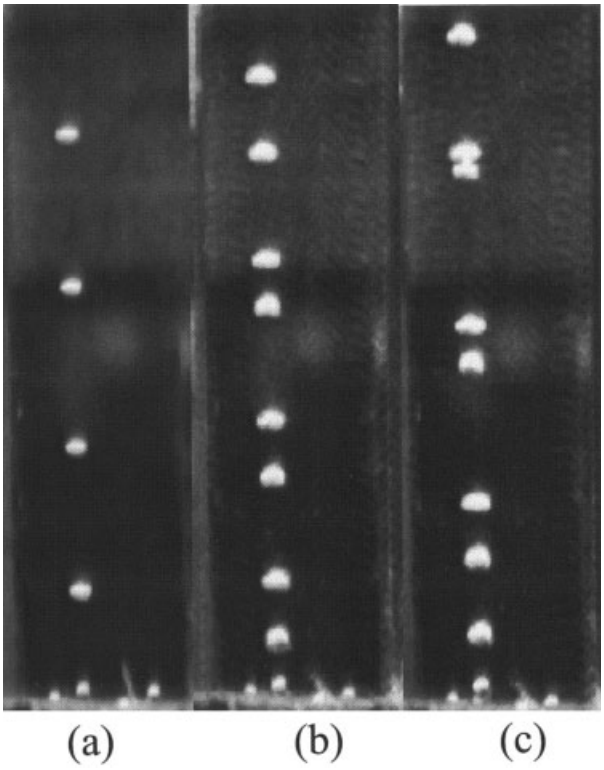

Figure 10. Experimental results on air bubble formation and rising in Paratherm NF heat-transfer fluid.

Nozzle size 0.4 cm I.D. and nozzle gas velocity (a) ~6.0 cm/s; (b) ~10.0 cm/s; (c) ~14 cm/s.

bubble images are taken under three different nozzle outlet velocities (approximately, 6.0, 10.0, and 14.0 cm/s) in Paratherm NF heat-transfer fluid. At a lower gas velocity, the bubble size is small and the rise velocity is uniform, so the bubble-bubble interaction is insignificant. As the gas velocity increases, the bubble size increases and the distance between bubbles decreases, indicating that the bubble-bubble interaction becomes important. The bubbles rise rectilinearly and, thus, the rise behavior is very different from that observed in the air-water system, as shown in Figure 11. Three different nozzle inlet velocities are used in the air-water experiments. It is clearly seen that, at all velocities used for nozzle air injection, bubbles rise in a zigzag path and a spiral motion of the bubbles prevails in air-water experiments. The simulation results on bubble formation and rise behavior conducted in this study closely resemble the experimental results.

Gas-liquid-solid fluidization

As noted earlier, to simulate the bubble motion in a gas-liquid bubble column accurately, fine grid sizes, 0.025 cm for air-water and 0.05 cm for air-Paratherm NF systems, should be used in the computation. This fine grid computation yields essentially the results of direct numerical simulation (DNS). These grid sizes are smaller than the size of the solid particle usually employed for the three-phase fluidized-bed operation. For the particle size of 0.08 cm used in the present simulation of a three-phase fluidized bed, the computational grid size is required to be no less than 0.2 cm in order to track both the bubble flow and the particle motion. Note that the system simulated in this study is a dilute liquid-solid bed with a minimum particle-particle collision and uniform particle distribution. Although a grid size of $\Delta > 10\ d_p$ as generally used in the Lagrangian simulation of fluid-particle flows is preferable, the grid size used under the current simulation of three-phase flows is acceptable. There is no numerical stability and convergence encountered in the computation. For simulation of the bubble formation in a gas-liquid bubble column, a coarse grid size of 0.2 cm in a $4 \times 4 \times 8$ cm^3 domain with $21 \times 21 \times 41$ grid points is used in this study. However, due to this large grid size used, without any turbulence model, the simulation cannot accurately track the discrete bubble formation process. Specifically, simulation without a consideration of the turbulent effects, the bubbles with distorted wake structure are seen to be connected like a jet above a nozzle. An SGS stress model is, thus, employed and incorporated into the code for subsequent simulation. The simulation of the gas-liquid bubble column system indicates that experimental results on a bubble formation in an air-Paratherm medium can be well described when C_s values are in a range of 1.0 to 1.2 with a grid size of 0.2 cm. Note that the values for the Smagorinsky coefficient for single-phase flow are at 0.1 ~ 0.2. The results are shown in Figure 12a.

Subsequently, simulations are performed for the air-Paratherm-solid fluidized-bed system with solid particles of 0.08 cm in diameter and 0.896 g/cm^3 in density. The solid particle

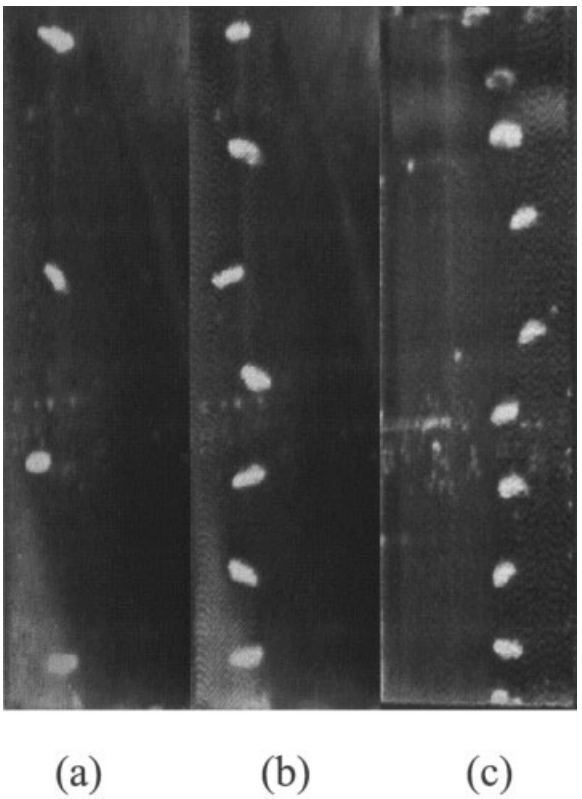

Figure 11. Experimental results on air bubble formation and rising in water.

Nozzle size 0.4 cm I.D. and nozzle gas velocity (a) ~6.0 cm/s; (b) ~10.0 cm/s; (c) ~14 cm/s.

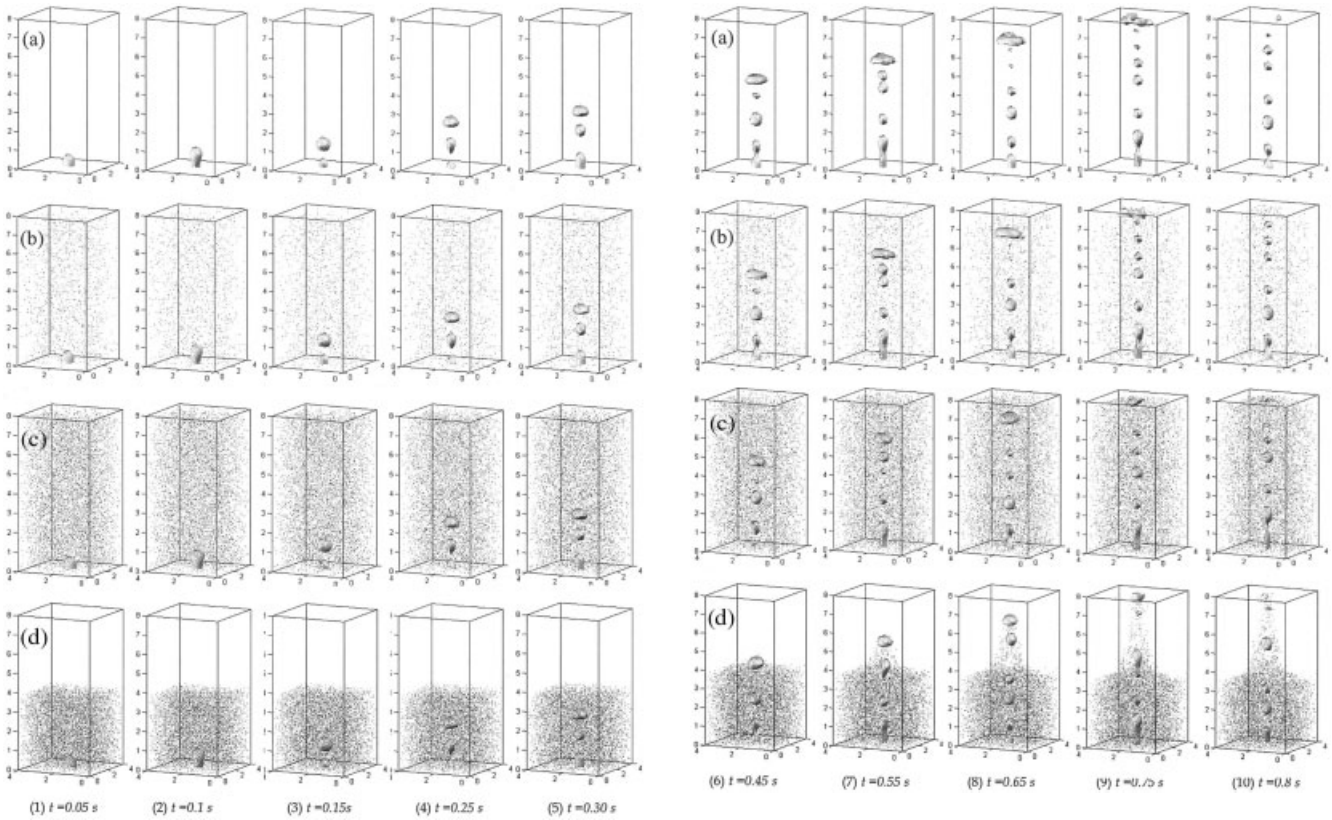

Figure 12. Simulation results of bubble formation and rising in Paratherm NF heat-transfer fluid with and without particles

Nozzle size 0.4 cm I.D., liquid velocity 0 cm/s, gas velocity 10 cm/s, and particle density 0.896 g/cm^3. (a) No particle; (b) 2,000 particles; (c) 8,000 particles; (d) 8,000 particles.

density is very close to the liquid density (0.868 g/cm^3). The boundary condition for the gas phase is inflow and outflow for the bottom and the top walls, respectively. Particles are initially distributed in the liquid medium in which no flows for the liquid and particles are allowed through the bottom and top walls. Free slip boundary conditions are imposed on four side walls. Specific simulation conditions for the particles are given as follows: Case b 2,000 particles randomly placed in a $4 \times 4 \times 8$ cm^3 column; Case c 8,000 particles randomly placed in a $4 \times 4 \times 8$ cm^3 column; and Case d 8,000 particles randomly placed in the lower half of the $4 \times 4 \times 8$ cm^3 column. The solids volume fractions are 0.42, 1.68 and 3.35%, respectively for Cases b, c and d.

The bubble formation process at different solids concentrations is shown in Figures 12b–12d and is compared with that without particles, as shown in Figure 12a. For the first 0.3 s, little change is observed in the bubble formation process for the three solids concentrations used in this simulation. After 0.4 s, however, significant changes can be found for the cases with high solids concentrations. This can be seen from the first bubble in each case. When the solid concentration is low or no solids are present, the first bubble grows on the orifice and connects to the second bubble. For the high solids concentration cases, the first bubble is not well connected to the second bubble. This is particularly true for Case d when the bubble rises into the solids-free region or freeboard region of the bed. The solid particle entrainment is clearly observed in Case d.

Simulations are also performed for the case with liquid flow. In the computation, solid particles with a density of 2.5 g/cm^3 are used. There are 2,000 particles which are initially randomly distributed in the lower half of a $4 \times 4 \times 16$ cm^3 column. The liquid flow is introduced at the bottom with a superficial velocity of 2.5 cm/s, where the solid particles are uniformly fluidized, yielding a uniform solids concentration of 0.42%. A single nozzle with a diameter of 0.4 cm and an outlet gas velocity of 10 cm/s introduces air bubbles into the liquid-solid fluidized bed. The computation is continued for 2 s while a quasi-steady state for the solid and bubble distribution is achieved after 1.7 s. The simulated bubble and particle positions are shown in Figure 13. As the figure shows, the entrainment of solid particles by bubbles takes place in the center region. The time sequence computation result reveals a circulatory motion of particles in the bed with upward flow in the center region and downward flow near the wall. This behavior results in a solids concentration profile along the horizontal direction, featuring a higher solids concentration in the center region especially behind each bubble, and a lower solids concentration near the wall region.

Multinozzle system with complex boundary conditions

The simulations on the bubble formation from multiple nozzles are performed. The computational domain is of an $8 \times 8 \times 16$ cm^3 column. Liquid is operated in a batch mode so that

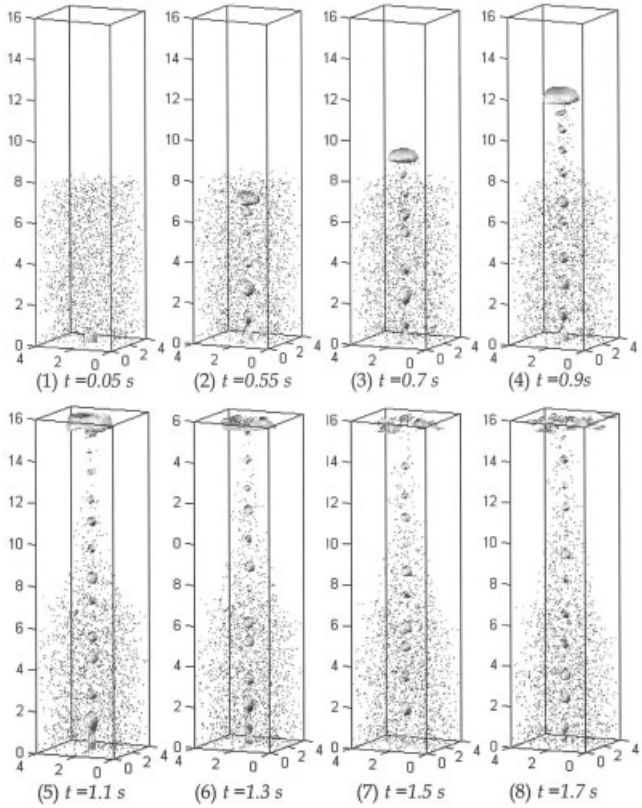

Figure 13. Simulation results of bubble formation and rising in Paratherm NF heat-trasnfer fluid with particles.

Nozzle size 0.4 cm I.D., liquid velocity 2.5 cm/s, gas velocity 10 cm/s, particle number 2,000, particle size 0.08 cm, and particle density 2.5 g/cm^3.

a free surface is imposed at a height of 12 cm. Paratherm NF heat-transfer fluid is used for the liquid phase. Four nozzles with a diameter of 0.4 cm are separated with a distance of 2.4 cm. The top wall is set as an outflow for the gas phase and the four side walls are free-slip boundaries.

The simulated bubble positions and the changes of the free surface are shown in Figure 14a and 14b, corresponding to two inlet gas velocities, that is, 6.0 and 10 cm/s, respectively. As shown in Figure 14a, even at a gas velocity as low as 6 cm/s, the bubble sizes and bubble distribution are not uniform, especially after bubbles have traveled for a distance. The formation frequencies for four nozzles are nearly the same for the first second. As calculation proceeds, bubble flows stop emerging from some nozzles and resume when flows from other nozzles stop. Bubble coalescence occurs and the bubble shapes near the nozzles and the free surface are not as spherical as in the other region. As the inlet gas velocity increases to 10 cm/s, bubble coalescence occurs more frequently in the nozzle region, and bubbles break up significantly near the free surface, as shown in Figure 14b.

Attempts have been made to simulate the multinozzle system using higher gas inlet velocities. For numerous sets of simulation, the bubbles are connected with each other as four jet-like gas flows formed in the nozzle region. In order to verify the simulation results, experiments on bubble formation and rising

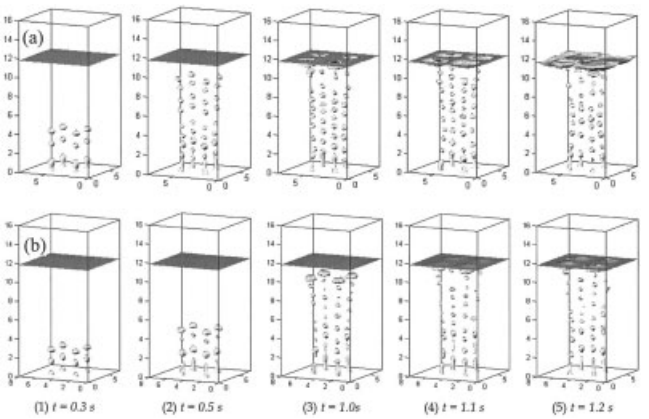

Figure 14. Simulation results of bubble formation from four nozzles and rising in Paratherm NF heat-transfer fluid.

Nozzle size 0.4 cm I.D. and nozzle gas velocity (a) ~6 cm/s; (b) ~10 cm/s.

behavior from multiple nozzles are conducted. Air is injected into the liquid bed through four nozzles with 0.4 cm I.D. and a displacement of 2.4 cm. Three outlet velocities (approximately, 6.0, 10.0, and 14.0 cm/s) are employed for gas nozzles. The experimental results are shown in Figure 15. At a low gas velocity, the bubble size is small and the bubble-bubble interaction is insignificant. As the gas velocity increases, the bubble

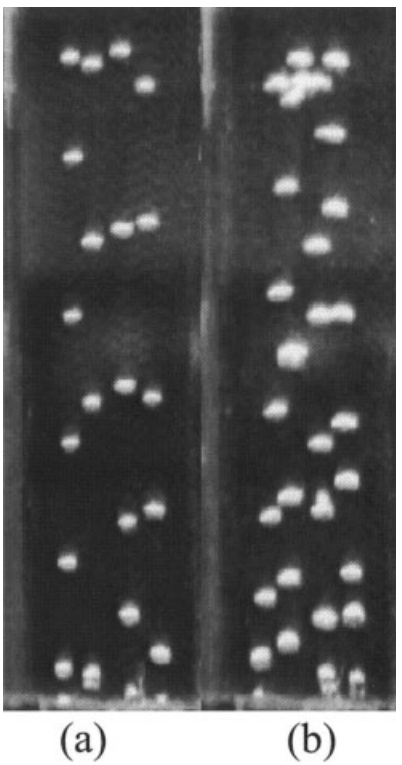

Figure 15. Experimental results on air bubble formation from four nozzles and rising in Paratherm NF heat-transfer fluid.

Nozzle size 0.4 cm I.D. and nozzle gas velocity (a) ~6.0 cm/s; (b) ~10.0 cm/s.

size increases and the bubbles tend to move toward the column center, implying that the bubble-bubble interaction is becoming important. However, bubble shapes are generally spherical and no jet-like gas flow is formed under the conditions similar to the simulations.

As one recalls that the bubble shape is tracked through a distance function and the bubble motion is simulated by the advection of the distance function, the thorough knowledge of the gas (in the bubble) and the liquid velocity fields is required for an accurate tracking of bubble motion. The present model uses the simple Smagorinsky SGS stress model to simulate the complex bubble wake flow structures. This model is identified in this study to be efficient for simple flows, such as a single bubble rising and bubble formation from a single nozzle. For the complex flow system with complicated initial and boundary conditions, further studies on the SGS model accounting for the bubble-induced turbulence are needed.

Concluding Remarks

The 3-D dynamic bubbling phenomena in a gas-liquid bubble column and a gas-liquid-solid fluidized bed are simulated using the level-set method for both the fine grid nodes and coarse grid nodes coupled with an SGS model for liquid turbulence. The computational scheme developed in this study captures the complex topological changes related to the bubble deformation, coalescence, and breakup in bubbling flows. The Smagorinsky SGS stress model is shown to be applicable in simulating the simple bubbling phenomena in a three-phase fluidized bed with values for the Smagorinsky coefficient significantly greater than those for single-phase flows. The effects of solids concentration on the bubble formation and rise behavior are also investigated. It is found that the bubbles are less coalesced in a fluidized bed with a higher solids concentration. A circulatory motion of particles with upward flow in the center region and downward flow near the wall, and a solids concentration distribution in the lateral direction in a gas-liquid-solid fluidized bed can be well simulated. For bubbling phenomena and for flow systems with complicated initial and boundary conditions, further studies on the SGS model in accounting for the bubble-induced turbulence are needed.

Acknowledgment

This work was supported, in part, by the National Science Foundation Grant CTS and the Ohio Supercomputer Center. The helpful assistance of Mr. Zhe Cui on the experimental work presented in Figures 4, 5, 10, 11, and 15 and the valuable comments of Mr. Yang Ge and Dr. Y-P Li in the preparation of this manuscript are gratefully acknowledged.

Notation

C_D = modified drag coefficient
D_{D0} = drag coefficient
C_s = Smagorinsky coefficient
d = distance function
d_p = diameter of particle
f_{am} = added mass force
f_d, F_D = fluid-particle interaction force
f_{dr} = drag force
f_σ, F_σ = surface tension force
g = gravitational acceleration
H_β = Heaviside function
l = length scale
$\boldsymbol{K}$ = curvature
m_p = mass of particle
p = pressure
Re_p = particle Reynolds number
S = shear strain rate
t = time
$\boldsymbol{V}$ = velocity
$\mathbf{x}$ = position vector

Greek letters

Γ = gas-liquid interface
Δ = grid size
β = half of the thickness of the interface
δ = δ function
ε = void fraction
λ = constant defined in Eq. 18
μ = molecular viscosity
ν_T = residual SGS eddy viscosity
ρ = density
σ = *surface tension
τ = viscous stress tensor, artificial time
ϕ = level-set function
Ω = cell volume

Subscripts and superscripts

g = gas phase
ij = cell index
k = particle index
l = liquid phase
p = particle
sg = sub-grid scale

Literature Cited

Anderson, T. B., and R. Jackson, "A Fluid Mechanical Description of Fluidized Beds," *I&EC Fund.,* **6,** 527 (1967).

Brackbill, J. U., D. B. Kothe, and C. Zemach, "A Continuum Method for Modeling Surface Tension," *J. Comp. Phys.,* **100,** 335 (1992).

Chen, Y.-M., and L.-S. Fan, "Bubble Breakage due to Particle Collision in a Liquid Medium: Particle Wettability Effects," *Chem. Eng. Sci.,* **44,** 2762 (1989a).

Chen, Y.-M., and L.-S. Fan, "Bubble Breakage Mechanisms due to Collision with a Particle in a Liquid Medium," *Chem. Eng. Sci.,* **44,** 117 (1989b).

Crowe, C. T., M. P. Sharma, and D. E. Stock, "The Particle-Source-in-Cell Method for Gas and Droplet Flow," *J. of Fluids Eng.,* **99,** 325 (1977).

Crowe, C., M. Sommerfeld, and Y. Tsuji, *Multiphase Flows with Droplets and Particles,* CRC Press, New York (1998).

Dandy, D. S., and L. G. Leal, "Buoyancy-driven Motion of a Deformable Drop through a Quiescent Liquid at Intermediate Reynolds Numbers," *J. Fluid Mech.,* **208,** 161 (1989).

Delnoij, E. J., A. M. Kuipers, and W. P. M. Van Swaaij, "Computational Fluid Dynamics Applied to Gas-Liquid Contactors," *Chem. Eng. Sci.,* **52,** 3623 (1997).

Fan, L.-S., and K. Tsuchiya, *Bubble Wake Dynamics in Liquid and Liquid-Solid Suspensions,* Butterworth-Heinemann, Stoneham, MA, (1990).

Grevskott, S., B. H. Sannæs, M. P. Dudukovic, K. W. Hjarbo, and H. F. Svendsen, "Liquid Circulation, Bubble Size Distributions, and Solids Movement in Two- and Three-Phase Bubble Columns," *Chem. Eng. Sci.,* **51,** 1703 (1996).

Harlow, F. H., and J. E. Welch, "Numerical Calculation of Time-Dependent Viscous Incompressible Flow of Fluid with Free Surface," *Physics of Fluid,* **8,** 2182 (1965).

Hirt, C. W., A. A. Amsden, and J. L. Cook, "An Arbitrary Lagrangian Eulerian Computing Method for all Speeds," *J. Comput. Phys.,* **14,** 227 (1974).

Hoomans, B. P. B., J. A. M. Kuipers, W. J. Briels, and W. P. M. Van Swaaij, "Discrete Particle Simulation of Bubble and Slug Formation in a Two-Dimensional Gas-Fluidized Bed: A Hard-sphere Approach," *Chem. Eng. Sci.,* **51,** 99 (1996).

Jackson, R., *The Dynamics of Fluidized Particles,* Cambridge University Press, New York (2000).

Kashiwa, B. A., N. T. Padial, R. M. Rauenzahn, and W. B. Vanderheyden, "A Cell-Centered ICE Method for Multiphase Flow Simulation," (Los Alamos National Laboratory Research Report, LA-UR-93-3922), *ASME Symp. on Numerical Methods for Multiphase Flows,* Lake Tahoe, NV (Jun. 19–23, 1994).

Kothe, D. B., and W. J. Rider, "Comments on Modeling Interfacial Flows with Volume-of Fluid Methods," *Los Alamos National Laboratory Research Report,* LA-UR-94-3384, (1995).

Lapin, A., and A. Lübbert, "Numerical Simulation of the Dynamics of Two-Phase Gas-Liquid Flows in Bubble Columns," *Chem. Eng. Sci.,* **49,** 3661 (1994).

Li, Y., J. Zhang, and L.-S. Fan, "Numerical Simulation of Gas-Liquid-Solid Fluidization Systems using a Combined CFD-VOF-DPM Method: Bubble Wake Behavior," *Chem. Eng. Sci.,* **54,** 5101 (1999).

McHyman, J., "Numerical Methods for Tracking Interfaces," *Physica D,* **12,** 396 (1984).

Monaghan, J., "Simulating Free Surface Flows with SPH," *J. Comput. Phys.,* **110,** 399 (1994).

Mudde, R. F., and O. Simonin, "Two- and Three-Dimensional Simulations of Bubble Plume using a Two-Fluid Model," *Chem. Eng. Sci.,* **54,** 5061 (1999).

Rowe, P. N., and G. A. Henwood, "Drag Forces in a Hydraulic Model of a Fluidized Bed," *Part 1., Trans. Inst. Chem. Eng.,* **39,** 43 (1961).

Scardovelli, R., and S. Zeleski, "Direct Numerical Simulation of Free-Surface and Interfacial Flow," *Ann. Rev. Fluid Mech.,* **31,** 567 (1999).

Smagorinsky, J., "General Circulation Experiments with the Primitive Equations: I. The Basic Equations," *Mon. Weather Rev.,* **91,** 99 (1963).

Sokolichin, A., and G. Eigenberger, "Gas-Liquid Flow in Bubble Columns and Loop Reactors: Part 1. Detailed Modeling and Numerical Simulation," *Chem. Eng. Sci.,* **49,** 5735 (1994).

Sokolichin, A., and G. Eigenberger, "Applicability of the Standard k-ε Turbulence Model to the Dynamic Simulation of Bubble Column: Part 1. Detailed Numerical Simulation," *Chem. Eng. Sci.,* **54,** 2273 (1999).

Sokolichin, A., G. Eigenberger, A. Lapin, and A. Lübbert, "Dynamic Numerical Simulation of Gas-Liquid Two-Phase Flows Euler/Euler versus Euler/Lagrange," *Chem. Eng. Sci.,* **52,** 611 (1997).

Sussman, M., and E. Fatemi, "An Efficient, Interface Preserving Level Set Re-distancing Algorithm and its Application to Interfacial Incompressible Fluid Flow," *SIAM J. Sci. Comput.,* **20,** 1165 (1999).

Sussman, M., E. Fatemi, P. Smereka, and S. Osher, "An Improved Level Set Method for Incompressible Two-Phase Flows," *Computers and Fluids,* **27,** 663 (1998).

Sussman, M., P. Smereka, and S. Osher, "A Level Set Approach for Computing Solutions to Incompressible Two-Phase Flow," *J. Comput. Phys.,* **114,** 146 (1994).

Unverdi, S. O., and G. Tryggvason, "A Front-Tracking Method for Viscous, Incompressible, Multi-Fluid Flows," *J. of Computational Physics,* **100,** 25 (1992a).

Unverdi, S. O., and G. Tryggvason, "Computations of Multi-Fluid Flows," *Physica D.,* **60,** 70 (1992b).

Wen, C. Y., and Y. H. Yu, "Mechanics of Fluidization," *Chem. Eng. Prog. Symp. Series,* **62,** 100 (1966).

Zenit, R., and M. Hunt, "Mechanics of Immersed Particle Collision," *J. of Fluids Eng.,* **121,** 179 (1999).

Zhang, J., L.-S. Fan, C. Zhu, R. Pfeffer, and D. Qi, "Dynamic Behavior of Collision of Elastic Spheres in Viscous Fluids," *Powder Technol.,* **106,** 98 (1999).

Manuscript received Oct. 4, 2002, and revision received June 16, 2003.